arXiv:1605.00054v2 [cond-mat.soft] 6 Aug 2016

Finsler geometry modelling of phase separation in multi-component membranes

Satoshi Usui and Hiroshi Koibuchi

Department of Mechanical and Systems Engineering
National Institute of Technology, Ibaraki College
Nakane 866, Hitachinaka, Ibaraki 312-8508, Japan

Abstract

A Finsler geometric surface model is studied as a coarse-grained model for membranes of three components, such as zwitterionic phospholipid (DOPC), lipid (DPPC) and an organic molecule (cholesterol). To understand the phase separation of liquid-ordered (DPPC rich) L_o and liquid-disordered (DOPC rich) L_d, we introduce a binary variable $\sigma(=\pm 1)$ into the triangulated surface model. We numerically determine that two circular and stripe domains appear on the surface. The dependence of the morphological change on the area fraction of L_o is consistent with existing experimental results. This provides us with a clear understanding of the origin of the line tension energy, which has been used to understand these morphological changes in three-component membranes. In addition to these two circular and stripe domains, a raft-like domain and budding domain are also observed, and the several corresponding phase diagrams are obtained.

Key words: Finsler geometry, Biological membranes, Surface orientation, Phase transition, Monte Carlo
PACS: 64.60.-i, 68.60.-p, 87.16.D-

1 Introduction

Membranes of multiple components, such as 1,2-dioleoyl-sn-glycero-3-phosphocholine (DOPC), dipalmitoylphosphatidylcholine (DPPC) and cholesterol, are receiving widespread attention because of their applications in many fields of science and technology, and numerous studies on the morphological changes have

Email address: koibuchi@mech.ibaraki-ct.ac.jp (Satoshi Usui and Hiroshi Koibuchi).

been conducted [1,2,3,4,5,6]. In these membranes, morphological changes are induced by a phase separation. Indeed, the phase separation causes domain formation and domain pattern transition between the liquid-ordered (L_o) and the liquid-disordered (L_d) phases. This domain pattern transition accompanies the morphological changes, such as the two circular domains, the stripe domain, the raft domain and the so-called budding domain [5,6]. The multiplicity of components, as in a glass transition [7], is essential for such a variety of morphologies. To date, these morphologies have been studied on the basis of the line tension energy [3,4] in the context of the Helfrich-Polyakov (HP) model for membranes [8,9]. The line tension energy is defined on the domain boundary and has an important role in the morphological changes [3,4].

However, the origin of the line tension energy is not well understood. In fact, it is unclear what type of internal structure is connected to the line tension energy until now. The problem that should be asked is where the line tension energy originates. Therefore, in this paper, we clarify and discuss the microscopic origin of the line tension energy.

To understand the origin of the line tension energy, we introduce new degrees of freedom $\sigma(=\pm 1)$ to represent the L_o and L_d phases. The Ising model Hamiltonian, which we call aggregation energy, for the variable σ is included in the general HP model Hamiltonian, where the "general" HP model refers to the HP model with a nontrivial surface metric $g_{ab}(\neq \delta_{ab})$. Note that the general HP model can be discretized on triangulated surfaces and becomes well defined only when it is treated in the context of Finsler geometry [10,11,12]. Moreover, note that our strategy towards the multi-component membrane in this paper is a coarse-graining of the detailed information on the chemical structures of DOPC, DPPC and cholesterol and on the interaction between them with the help of the variable σ and HP surface model. In addition, from the viewpoint of modelling, it is very natural to extend the Hp model to the general HP model for explaining the morphological changes in multi-component membranes. Indeed, the HP model is considered as a straight forward extension of the linear chain model for polymers [13].

The remainder of this paper is organized as follows. In Subsection 2.1, we introduce the continuous Hamiltonian, which is identical to the Polyakov Hamiltonian [8]. In Subsection 2.2, we introduce the two-component surface model, which is defined by including the aggregation energy in the Hamiltonian of the FG surface model. The aggregation energy is defined by the variable σ, which is introduced to label the triangles with L_o and L_d. The Monte Carlo (MC) technique is briefly discussed in Section 3, and the MC results are presented in Section 4. Finally, we summarize the results in Section 5. In Appendix A, we describe the technical details of the FG modelling. In Subsection A.1, the discretization of the continuous model introduced in Subsection 2.1 is described, and a discrete model is obtained. From this discrete model, we obtain the

model for two-component membranes by imposing a constraint on the metric function. In A.2, we show that the models constructed in A.1 are ill defined in the conventional modelling and that the models become well defined only in the context of Finsler geometry modelling.

2 Two-component surface model

2.1 Continuous surface model

We begin with a continuous surface model, which is defined by the Polyakov Hamiltonian or the Gaussian energy S_1 for membranes and the bending energy S_2 with a metric $g(x)$, where $x=(x_1,x_2)$ is the local coordinate of the two-dimensional parameter space M [14]. Both of the energies are defined by the surface position $\mathbf{r}(\in \Re^3)$ such that

$$
\begin{aligned}
S_1 &= \int \sqrt{g} d^2x g^{ab} \frac{\partial \mathbf{r}}{\partial x_a} \cdot \frac{\partial \mathbf{r}}{\partial x_b}, \\
S_2 &= \frac{1}{2} \int \sqrt{g} d^2x g^{ab} \frac{\partial \mathbf{n}}{\partial x_a} \cdot \frac{\partial \mathbf{n}}{\partial x_b},
\end{aligned} \tag{1}
$$

where g is the determinant of the 2×2 matrix g_{ab} of the metric function and g^{ab} is its inverse [14]. The symbol $\mathbf{n}$ denotes a unit normal vector of the surface. Both S_1 and S_2 are conformally invariant. The conformal invariance is a property in which a scale change $g_{ab}(x) \to f(x) g_{ab}(x)$ is not reflected in both S_1 and S_2 for any positive function f. Two metrics g and g' are called "conformally equivalent" if a function $f(x)$ exists such that $g'_{ab}=f(x)g_{ab}$ [14].

For the case where $g_{ab}(x)$ is given by the Euclidean metric $g_{ab}=\delta_{ab}$ (or the induced metric $g_{ab}=\partial_a \mathbf{r} \cdot \partial_b \mathbf{r}$), the surface shape $\mathbf{r}$ in $\Re^3$ is treated from the perspective of statistical mechanics. These are the HP model [8,9] corresponding to polymerized membranes, and the HP model and the Landau-Ginzburg model [15] have been thoroughly investigated [16,17,18,19,20,21,22].

2.2 Discrete model

First, in this subsection, let us introduce a new degree of freedom σ, which has only two-different values ($\sigma=\pm 1$), on the triangulated lattice (see Figure A.1 in Appendix A). We assume that the variable σ_i is defined on the triangle Δ_i, and moreover, the values of σ_i correspond to two different phases, namely, the liquid-ordered (L_o) and the liquid-disordered (L_d) phases, such that

$$\sigma(\Delta) = \begin{cases} 1 & (\Delta \in L_o) \\ -1 & (\Delta \in L_d)\,. \end{cases} \tag{2}$$

This definition of σ implies that every triangle is labelled by the value of σ, and therefore, σ represents the phase (or domain) to which the triangle Δ belongs.

We now introduce a discrete Hamiltonian for multi-component membranes. The technical details of the discretization of the continuous Hamiltonian S_1 and S_2 introduced in Subsection 2.1 are described in Appendix A.1, and the discrete expressions for S_1 and S_2 are given in Eq. (A.8) in Appendix A.1. Using these S_1 and S_2, we have the total Hamiltonian S such that

$$\begin{aligned} &S(\mathbf{r},\sigma) = \lambda S_0 + S_1 + \kappa S_2, \\ &S_0(\sigma) = \sum_{ij} (1 - \sigma_i \cdot \sigma_j)\,, \\ &S_1(\mathbf{r},\sigma) = \sum_{ij} \gamma_{ij}(\sigma)\ell_{ij}^2, \\ &S_2(\mathbf{r},\sigma) = \sum_{ij} \kappa_{ij}(\sigma)\,(1 - \mathbf{n}_i \cdot \mathbf{n}_j)\,, \end{aligned} \tag{3}$$

where $S(\mathbf{r},\sigma)$ denotes that the Hamiltonian depends on the variables $\mathbf{r}(\in \Re^3)$ and σ. The three-dimensional vector $\mathbf{r}$ denotes the vertex position of the triangulated lattice. The energy λS_0 is called the *aggregation energy*. When $\lambda \to 0$, the variable σ becomes random, and this random configuration simply corresponds to the coexistence phase, where L_o and L_d are not separated. Conversely, when λ becomes sufficiently large, two neighbouring σs have the same σ, and this configuration corresponds the phases where L_o and L_d are separated. As described above, the second and third terms S_1 and S_2 in S are the discrete Hamiltonians corresponding to the continuous ones introduced in 2.1. The coefficient κ of S_2 is the bending rigidity and has units of $[1/k_BT]$, where k_B and T are the Boltzmann constant and the temperature, respectively. In this paper, we assume that $k_BT = 1$. The symbol $\mathbf{n}_i$ in S_2 expresses a unit normal vector of the triangle i. The symbols $\gamma_{ij}(\sigma)$ and $\kappa_{ij}(\sigma)$ denote that γ_{ij} and κ_{ij} depend on the variable σ, and this dependence arises from an interaction between σ and $\mathbf{r}$. The interaction between σ and $\mathbf{r}$ is defined by the function ρ such that

$$\rho(\Delta) = \begin{cases} c & (\Delta \in L_o \Leftrightarrow \sigma(\Delta) = 1) \\ 1 & (\Delta \in L_d \Leftrightarrow \sigma(\Delta) = -1)\,, \end{cases} \tag{4}$$

where c is a parameter that should be fixed at the beginning of the simulations.

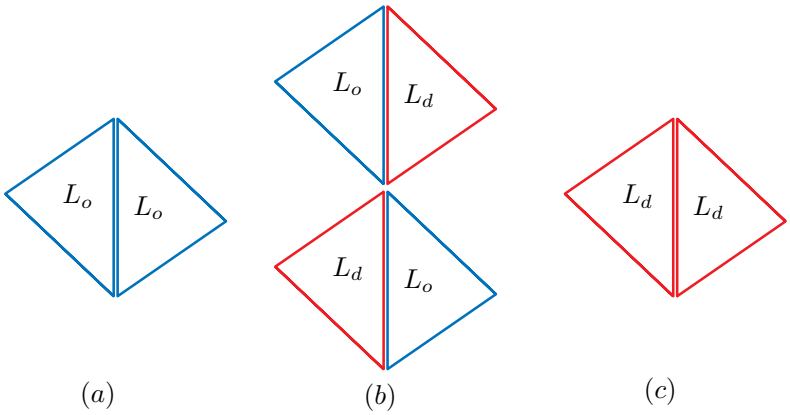

Fig. 1. The dependence of κ_{ij} and γ_{ij} on four possible combinations of L_o and L_d: (a) $\kappa_{ij}=\gamma_{ij}=(c+c^{-1})/2$ on (L_o, L_o), (b) $\kappa_{ij}=\gamma_{ij}=(2+c+c^{-1})/4$ on (L_o, L_d), and (c) $\kappa_{ij}=\gamma_{ij}=1$ on (L_d, L_d). $(L_{o,d}, L_{o,d})$ correspond to the bonds represented by the duplicated lines.

From this definition of $\rho(\Delta)$ and Eq. (A.9) in Appendix A.1, we have (see Figure 1)

$$\gamma_{ij} = \kappa_{ij} = \frac{c_i + c_j}{4} = \frac{1}{4}\left(\rho_i + \frac{1}{\rho_i} + \rho_j + \frac{1}{\rho_j}\right)$$
$$= \begin{cases} (c + c^{-1})/2 & [\sigma_i = \sigma_j = 1 \ : \ (L_o, L_o)] \\ (2 + c + c^{-1})/4 & [\sigma_i\sigma_j = -1 \ : \ (L_o, L_d)] \\ 1 & [\sigma_i = \sigma_j = -1 \ : \ (L_d, L_d)]\,. \end{cases} \tag{5}$$

These expressions represent how the effective surface tension γ_{ij} and bending rigidity $\kappa\kappa_{ij}$ depend on the position of the bond ij, which is one of the three domain boundary bonds (L_o, L_o), (L_o, L_d), and (L_d, L_d). The symbol (L_o, L_d) refers to the bond shared by the two neighbouring triangles of the L_o and L_d phases (see Fig. 1). Note that only (L_o, L_d) corresponds to the bond on the domain boundary, and the other two correspond to the bonds inside the domains L_o and L_d. From the expressions of γ_{ij} and κ_{ij} in Eq. (5), we understand that the dependence of γ_{ij} and κ_{ij} on the domains and their boundary is automatically determined. Thus, this expression is one of the most interesting outputs of the model in this paper. The values of γ_{ij} and κ_{ij} depend on the parameter c, which is an input parameter.

In Figure 2, $\gamma_{ij}(=\kappa_{ij})$ for (L_o, L_o), (L_o, L_d), and (L_d, L_d) are plotted as functions of c in the region $1 \le c$. The expressions of γ_{ij} and κ_{ij} in Eq. (5) are symmetric under the exchange $c \leftrightarrow 1/c$, and therefore, we use the value of c rather than $1/c$ to represent γ_{ij} and κ_{ij}. The curve of $\gamma_{ij}(=\kappa_{ij})$ against c is almost linear except for the region $c \simeq 1$. The dashed vertical lines in the figure correspond to $c=5$ and $c=8.37$, which are assumed in the simulations.

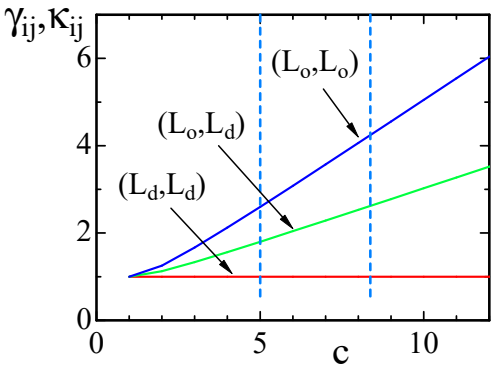

Fig. 2. Three different values of γ_{ij} and κ_{ij} vs. c, where $\kappa_{ij}=\gamma_{ij}=(c+c^{-1})/2$ on the (L_o, L_o) boundary, $\kappa_{ij}=\gamma_{ij}=(2+c+c^{-1})/4$ on the (L_o, L_d) boundary, and $\kappa_{ij}=\gamma_{ij}=1$ on the (L_d, L_d) boundary. The dashed lines denote the values of c assumed in some of the simulations.

The fluid surface model is defined by the sum over all possible triangulations $\sum_{\mathcal{T}}$ in the partition function such that

$$Z(\lambda,\kappa)=\sum_{\mathcal{T}}\int'\prod_{i=1}^{N}d\mathbf{r}_i\exp\left[-S(\mathbf{r},\sigma)\right], \tag{6}$$

where the prime in $\int'$ denotes that the center of mass of the surface is fixed at the origin of $\Re^3$ to protect the surface translation. The dynamical triangulation, denoted by $\sum_{\mathcal{T}}$, is performed using the bond flip technique [23,24,25,26,27,28]. Due to this bond flip, the vertices can freely diffuse over the surface, where two neighbouring triangles merge and split into two different ones and the total number of triangles remains unchanged in this process. Therefore, not only the vertices but also the triangles diffuse over the surface.

Note that the metric variable, or in other words, the function ρ, is not summed over (or integrated out) in Z; hence, strictly speaking, it is not a dynamical variable. However, the metric variable ρ is effectively considered as dynamical in the sense that ρ changes its value on the surface due to the diffusion of triangles.

Moreover, note that the aggregation energy λS_0 simply corresponds to the line tension energy in Refs. [3,4]. Indeed, the energy $1-\sigma_i\cdot\sigma_j$ at the bond ij has a non-zero positive value only when the bond is on the domain boundary between L_o and L_d. More precisely, S_0 is proportional to the total number of bonds that form the domain boundary because the mean bond length is constant (or non-zero finite) on the boundary.

We comment on the reason why λS_0 is considered as the line tension energy in more detail. First, the fact that the mean bond length becomes constant is understood from the scale-invariant property of the partition func-

tion Z in Eq. (6). Indeed, we have $\langle S_1\rangle/N = 3/2$ [29]. It is easy to see that this relation is satisfied: Z is independent of the scale change $\mathbf{r} \to \alpha\mathbf{r}$ for arbitrary $\alpha \in \Re$, and therefore, we have $dZ(\alpha)/d\alpha|_{\alpha=1} = 0$. Because $Z(\alpha) = \alpha^{3N-1} \sum_{\mathcal{T}} \int' \prod_{i=1}^{N} d\mathbf{r}_i \exp\left[-S(\alpha\mathbf{r})\right]$, $S(\alpha\mathbf{r}) = \lambda S_0 + \alpha^2 S_1 + \kappa S_2$, we have $S_1/N = 1.5$ for sufficiently large N. The relation $\langle S_1\rangle/N = 3/2$ means that $\langle \gamma_{ij}\ell_{ij}^2\rangle$ is constant. This implies that $\langle \ell_{ij}^2\rangle$ and hence $\langle \ell_{ij}\rangle$ becomes constant. This constant $\langle \ell_{ij}\rangle$ varies depending on whether the bond ij belongs to L_o, L_d or the boundary between L_o and L_d because the coefficient γ_{ij} varies depending on these domains and domain boundary as in Eq. (5). For this reason and because $\langle \gamma_{ij}\ell_{ij}^2\rangle =$ constant, we understand that the bond length on the boundary between L_o and L_d becomes well defined (or non-zero finite). Importantly, the mean bond length is expected to be finite, although it fluctuates around the mean value and the mean value itself varies depending on the domains or the domain boundary. Therefore, λS_0 is considered to be an extension of the line tension energy because S_0 is proportional to the length of the phase boundary if the two phases are clearly separated as the domains L_o and L_d at least.

The remaining problem to be clarified is how the domain boundary is formed on the triangulated surfaces. During experiments, the area fraction of L_o (and L_d) is fixed [3]. Hence, in our model the total number of triangles N_T^o for $\sigma = 1$ (and N_T^d for $\sigma = -1$) is fixed, where the total number of triangles

$$N_T = N_T^o + N_T^d \tag{7}$$

is also fixed to be constant (because $N_T = 2N - 4$ and the total number N of vertices is fixed). The relation between the area fraction of L_o and the fraction of N_T^o will be described in the next section. Another constraint imposed on the triangles in our model is that the value of σ_i of triangle i remains unchanged for all i during the simulations. Therefore, the triangles themselves have to diffuse over the surface to form the L_o and L_d domains. This triangle diffusion is numerically possible on the dynamically triangulated surfaces, which are called triangulated fluid surfaces, via the Monte Carlo (MC) technique with dynamical triangulation, as described above [23,24,25,26,27,28].

The function $\rho(\Delta)$ in Eq.(4) characterizes the difference between the phases L_o and L_d of Δ, and these two different phases are labelled by the variable $\sigma(\Delta)$ as in Eq. (2). Therefore, the model in this paper is limited to membranes with two-component domains, however, the modelling technique is applicable to membranes with multi-component domains. Here we comment on how to extend the model to a n-component model. To extend the 2-component model, we have to define the value of $\rho(\Delta)$ for the n-component model such that $\Delta \in L_i (1 \le i \le n)$ (see Eq.(4)), where $\{L_1, L_2, \cdots, L_n\}$ is the set of domains assumed. In this case, the variable $\sigma(\Delta)$ should be n components, and therefore, the corresponding energy term λS_0 in Eq. (3) should also be extended.

The Hamiltonian of n-states Potts model, for example, can be used for S_0. Hamiltonians of continuous models, such as the Heisenberg spin model, can also be assumed for S_0, where the continuous variable $\sigma(\Delta)$ should be connected in one-to-one correspondence with the n-component function $\rho(\Delta)$ (see Eq.(4)). In these n-component models, the energy λS_0 is still expected to play the role of line tension energy between two different domains, because λS_0 becomes zero (nonzero) if the phases of two neighbouring triangles are identical to (different from) each other. The parameters κ_{ij} and γ_{ij} are given by the same expression in Eq. (A.9), however, the final expression of these parameters in the n-component model are in general different from those in Eq. (5) because of the dependence of the parameters on the definition of ρ_i. Indeed, the parameters κ_{ij} and γ_{ij} in the n-component model will be different from those determined by the single parameter c in the two-component model.

3 Monte Carlo technique

The canonical Metropolis technique is used [30,31]. The vertex position $\mathbf{r}$ is updated such that $\mathbf{r}' = \mathbf{r} + \delta\mathbf{r}$. The symbol $\delta\mathbf{r}$ denotes a random three-dimensional vector in a sphere of radius R. The new position $\mathbf{r}'$ is accepted with probability $\mathrm{Min}[1, \exp(-\delta S)]$, where $\delta S = S(\mathrm{new}) - S(\mathrm{old})$. The radius R of the small sphere is fixed such that the acceptance rate for the update of $\mathbf{r}$ is approximately equal to 50%.

The triangulation $\mathcal{T}$ is updated using the bond flip technique, as described in the previous section [23,24,25,26,27,28]. We use the same technique used in Refs. [23,24,25,26,27,28], except for the following constraint. In the bond flip, the two neighbouring triangles of the bond change to a new pair of triangles such that the fraction ϕ_0 of L_o (or L_d) remains unchanged, where ϕ_0 is defined by

$$\phi_0 = N_T^o / N_T. \tag{8}$$

More precisely, if the two triangles have the same value of σ prior to the bond flip, then the new values of σ for the new triangles are fixed to be the same as the old one. However, if the values of σ are different from each other before the bond flip, then the new values are also fixed randomly to be different. Only through this process is the variable σ updated. Due to this update of σ through the dynamical triangulation, the function ρ changes, and hence, a domain structure of L_o (or L_d) is formed on the surface.

We comment on the relation between the fraction ϕ_0 and the area fraction of L_o. As described in the previous section, the mean triangle areas a_o and a_d in the domains L_o and L_d are constant because of the scale invariance of

Z. Therefore, the area fraction of L_o can be written as $N_T^o a_o/(N_T^o a_o + N_T^d a_d)$, which is identical to $\phi_0 = N_T^o/N_T$ if $a_o = a_d$. However, the area fraction of L_o is not always reflected in the fraction ϕ_0 if $a_o \neq a_d$.

The initial configuration for the simulations is fixed to be the random phase, where the L_o (or L_d) triangles are randomly distributed on the surface under a constant ratio ϕ_0. This random state corresponds to the two-phase coexistence configuration.

A single Monte Carlo sweep (MCS) consists of N updates of $\mathbf{r}$ and of N updates for the bond flips. The total number of MCS that should be performed depends on the parameters; it ranges from approximately $1{\times}10^8$ to $8{\times}10^8$. The numbers of MCS for almost all simulations are $2{\times}10^8 \sim 3{\times}10^8$. The simulations at the phase boundaries are relatively time consuming in general because the domain structure and hence the surface shape changes very slowly at these boundaries. The total number of vertices N is fixed to $N = 5762$ in this paper.

4 Simulation results

Two types of models, which are denoted as model 1 and model 2, are simulated. The Gaussian energy $S_1 = \sum_{ij} \ell_{ij}^2$ of the canonical surface model is assumed for model 1. From this assumption, the effective surface tension γ_{ij} for model 1 is $\gamma_{ij} = 1$. Model 2 is the same as the one introduced in Section 2.2. The Gaussian energy S_1 and the parameters γ_{ij} and κ_{ij} for model 1 and model 2 are presented in Table 1.

Table 1
The Gaussian bond potential S_1 and the parameters γ_{ij} and κ_{ij} assumed in model 1 and model 2. (see Eq. (A.9) in Appendix A.1)

	S_1	γ_{ij}	κ_{ij}
model 1	$S_1 = \sum_{ij} \ell_{ij}^2$	1	$(c_i + c_j)/4$
model 2	$S_1 = \sum_{ij} \gamma_{ij} \ell_{ij}^2$	$(c_i + c_j)/4$	$(c_i + c_j)/4$

In model 1, the surface shape is influenced only by κ_{ij} because $\gamma_{ij} = 1$. In contrast, in model 2, the coefficient γ_{ij} influences the surface size because S_1 in Eq. (3) has the unit of length squares. Indeed, as described in Section 2, from the scale invariance of Z, we have $\langle S_1 \rangle / N = 3/2$ [29], and therefore, ℓ_{ij}^2 deviates from the constant expected from this relation if the constraint $\gamma_{ij} = 1$ is not imposed on γ_{ij}. For example, if γ_{ij} is large (small), then ℓ_{ij}^2 becomes small (large). Therefore, due to this dependence of ℓ_{ij}^2 on γ_{ij}, the size of the triangles in model 2 depends on the domains. By contrast, there is no dependence of ℓ_{ij}^2 on the domains in model 1, where $\gamma_{ij} = 1$ over the entire surface.

The input parameters for the simulations are λ, κ, c, and ϕ_0, where c is the value of the function ρ in Eq. (4) and determines γ_{ij} and κ_{ij}. The parameter ϕ_0 defined by Eq. (8) is identical to the area fraction in model 1, whereas it differs from the area fraction in model 2 because the triangle area is not uniform in model 2. More precisely, the mean triangle area in the L_o domain is different from that in the L_d domain in model 2. In Table 2, we show the parameters assumed in the simulations. The values of κ_{ij} corresponding to the input c are listed in Table 3.

Table 2
The input parameters λ, κ, c and ϕ_0 for the simulations.

	λ	κ	c	ϕ_0
model 1	$0.03 \leq \lambda \leq 0.5$	7	5	$0.3 \leq \phi_0 \leq 0.8$
model 2	$0.03 \leq \lambda \leq 0.8$	10	8.37	$0.7 \leq \phi_0 \leq 0.9$
model 2	3	$7 \leq \kappa \leq 15$	5	$0.65 \leq \phi_0 \leq 0.95$

Table 3
The input parameter c automatically defines the values of κ_{ij} and γ_{ij}, where $\gamma_{ij}=1$ for model 1 and $\gamma_{ij}=\kappa_{ij}$ for model 2.

	c	$\kappa_{ij}(L_o, L_o)$	$\kappa_{ij}(L_o, L_d)$	$\kappa_{ij}(L_d, L_d)$
model 1	5	2.6	1.8	1
model 2	8.37	4.24	2.62	1
model 2	5	2.6	1.8	1

4.1 Model 1

We first show a phase diagram on the $\lambda - \phi_o$ plane in Figure 3. The parameters κ and c are fixed to $\kappa = 7$ and $c = 5$, as shown in Table 2, and λ is varied in its relatively small region. The dots (•) are the data points where we perform the simulations to construct the phase diagram. We find that the two phases L_o and L_d are not separated in the region $\lambda < 0.1$, the domain pattern is random, and the surface is almost spherical, as observed in the snapshots. In contrast, in the region $\lambda > 0.1$, L_o and L_d are clearly separated, and the two circular domains and the stripe domain appear. The domain structure depends on the value of ϕ_0, and the corresponding surface morphology appears to be almost discontinuously separated on the phase diagram. We observe that the two circular domains change to the stripe domain as the fraction ϕ_0, which is identical with the area fraction of L_o, increases for constant λ. This result is consistent with the experimental results reported in [3], where the area fraction of L_o is changed. The two circular domains and the stripe domain correspond

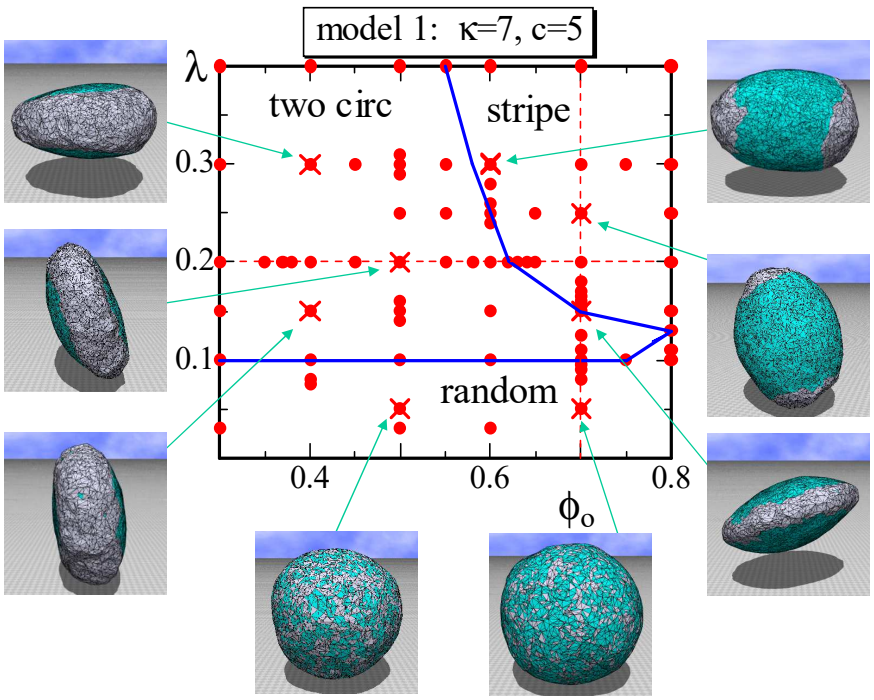

Fig. 3. A phase diagram of model 1 on the $\lambda - \phi_o$ plane at $\kappa = 7$ and $c = 5$, and the snapshots of surfaces obtained at the points indicated by the symbol ($\times$). The solid lines denote the phase boundaries, and the dashed lines denote the positions for the simulations for Figures 4 (a),(b),(c). The solid circles ($\bullet$) denote the data points of the simulations for the phase boundaries. The two circular domains and the stripe domain correspond to the L_o phase, which is DPPC rich. The two separated domains in the surface of striped domain and the connected domain in the surface of two circular domains correspond to the L_d phase, which is DOPC rich.

to the L_o phase, where κ_{ij} is higher than those of both the L_d domain and the boundary, as shown in Table 1. For this reason, the L_o domain is relatively smooth compared to the L_d domain. The ratio $\kappa_{ij}(L_o, L_o)/\kappa_{ij}(L_d, L_d)(=2.5\sim 4.3)$ assumed in the simulations is comparable to or slightly larger than the experimental prediction $\kappa_{ij}(L_o, L_o)/\kappa_{ij}(L_d, L_d)(=1\sim 4)$ [3].

Next, to show the dependence of the surface size on the parameters, we define semi-axis lengths D_1, D_2, and D_3 of the surface such that $D_1 > D_2 > D_3$ as in Figure 5. D_1 and D_2, D_3 correspond to the major and minor axes, respectively. The surface of the stripe domain corresponds to the so-called prolates, where $D_1 > D_2 \simeq D_3$ is expected. It is also expected that $D_1 \simeq D_2 > D_3$ in the so-called oblates, which corresponds to the surface shape of the two circular domains. Therefore, the surfaces with the stripe and two circular domains can be distinguished by the minor axis D_2.

We plot D_2 vs. ϕ_0 in Figure 4(a), where $\lambda = 0.2$. As shown, D_2 discontinuously changes against ϕ_0 at the phase boundary between the two circular and stripe domains. From the plot of D_2 vs. λ in Figure 4(b), we also observe that D_2

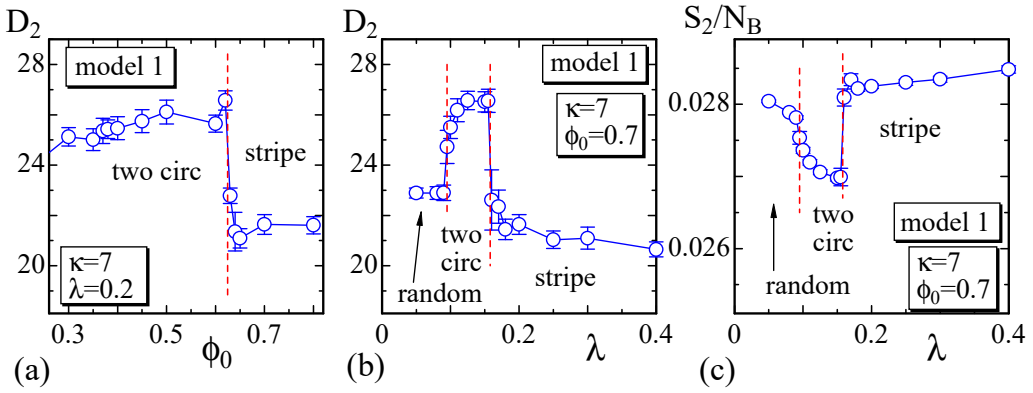

Fig. 4. (a) The size D_2 vs. ϕ_0 at $\lambda = 0.2$, (b) D_2 vs. λ at $\phi_0 = 0.7$, and (c) the bending energy S_2/N_B vs. λ at $\phi = 0.7$. These are calculated on the dashed horizontal and vertical lines in Figure 3. The minor axis D_2 and the bending energy S_2/N_B change almost discontinuously and smoothly at the phase boundaries, which are denoted by the vertical dashed lines.

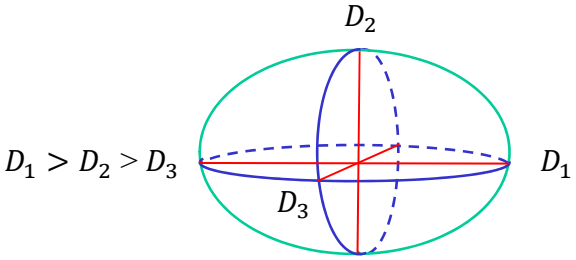

Fig. 5. The surface size is characterized by three diameters D_1, D_2, and D_3, where $D_1 > D_2 > D_3$. The three axes are perpendicular to each other.

discontinuously changes at the same phase boundary. The bending energy S_2/N_B in Figure 4(c) also discontinuously changes at this boundary, and this result indicates that this morphological change is considered as a first-order transition. However, note that the change of the morphology at this phase boundary is relatively smooth. In fact, one circular domain surface, which is not shown as a snapshot in Figure 3, can be observed at the boundary. This implies that the stripe domain surface and one circular domain surface have the same bending energy, or in other words, the bending energy is degenerate. Additionally, note that the phase boundary between the two circular and random domains appears to be continuous. This means that the shape of the two circular domain surface continuously changes to the random domain surface. At this phase boundary, the surface shape continuously changes from pancake to sphere.

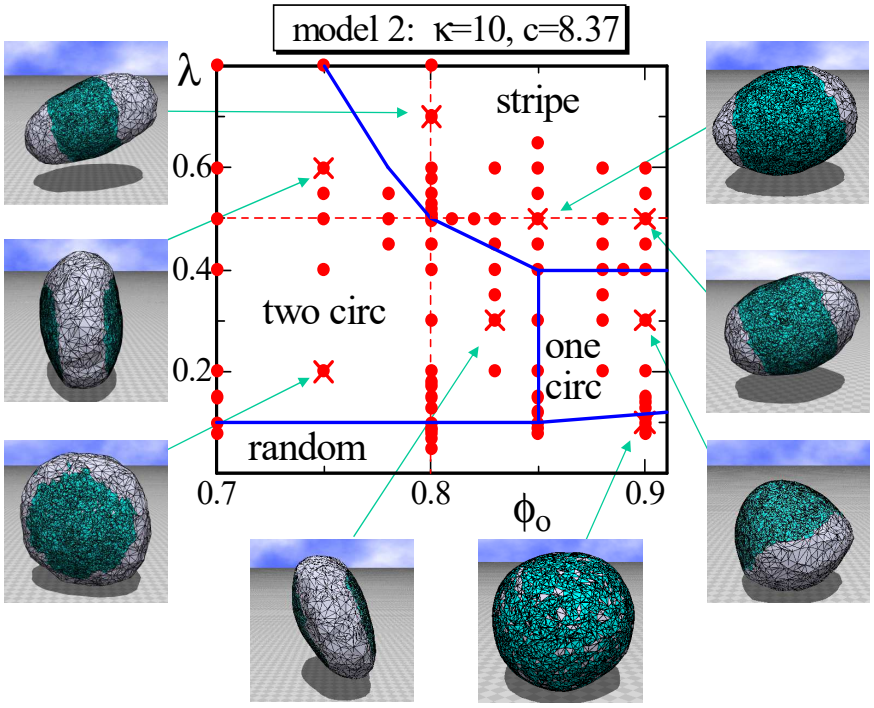

Fig. 6. A phase diagram of model 2 on the $\lambda - \phi_o$ plane at $\kappa = 10$ and $c = 8.37$ and the snapshots of surfaces. The solid lines on the phase diagram denote the phase boundaries, and the dashed lines denote the positions for the simulations for Figures 7 (a),(b),(c). The solid circles (●) denote the data points of the simulations for the phase boundaries.

4.2 Model 2

In model 2, not only κ_{ij} but also γ_{ij} depend on the domain (or the domain boundary) whether it is L_o or L_d. For this reason, the area of the triangles in the L_o domain becomes considerably smaller than that in the L_d domain. Therefore, the fraction ϕ_0 does not reflect the area fraction of L_o in this case. In fact, it is easy to see that the area fraction of L_o in the snapshots at $\phi_0 = 0.9$ in Figure 6 is much smaller than 90%. Nevertheless, the phase diagram on the $\lambda - \phi_0$ plane in Figure 6 appears almost the same as that in Figure 3. The only difference between the two phase diagrams is the appearance of one circular domain phase, denoted by "one circ" in Figure 6. This one circular phase is stable, where "stable" means that the surface domain remains unchanged against a small variation of the parameters inside the phase boundary. This is in sharp contrast to the one circular domain surfaces observed at the region close to the boundary between the two circular and stripe domains because these one circular surfaces are very sensitive to the parameter variation and hence "unstable". The shape of the one circular surface in the one circular region is almost spherical, such as the one shown in Figure 6, and this result is in contrast to the result in Ref. [4], where the one circular phase is separated into

two phases: the prolate and oblate phases. One possible reason for why only a spherical surface appears in the one circular domain in Figure 6 is because the L_o domain is hardly bent due to the high ratio $\kappa_{ij}(L_o, L_o)/\kappa_{ij}(L_d, L_d) = 4.24$, which is slightly larger than the one $1 < \kappa_{ij}(L_o, L_o)/\kappa_{ij}(L_d, L_d) < 3$ assumed in Ref. [4]. The parameters assumed on this plane are $\kappa = 10$ and $c = 8.37$, which are listed in Table 1.

The simulations are also performed on the $\lambda - \phi_0$ planes for larger κ, such as $\kappa = 15$ and $\kappa = 20$, and with $c = 8.37$. The phase diagrams obtained in these simulations are (not shown) relatively close to that shown in Figure 6; however, surfaces with three or four circular domains appear in the lower λ region in the two circular domain phase. The bending energy κS_2 of the three or four domains is lower than that of the two circular domain; moreover, the aggregation energy λS_0 of these multi-circular domains is larger than that of the two circular domain. These are the reasons for the appearance of the three or four domains only in the relatively small λ region in the simulations with relatively large κ.

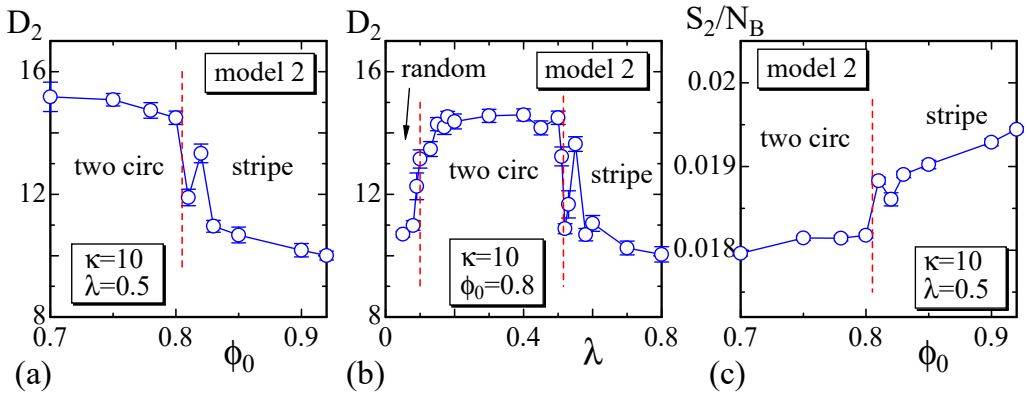

Fig. 7. (a) The size D_2 vs. ϕ_0 at $\lambda = 0.5$, (b) D_2 vs. λ at $\phi_0 = 0.8$, and (c) the bending energy S_2/N_B vs. ϕ_0 at $\lambda = 0.5$. These are calculated on the dashed horizontal and vertical lines in Figure 6. The size of the surface changes almost discontinuously and smoothly at the phase boundaries, which are denoted by the dashed lines.

To observe the variation of the surface size at the phase boundaries, we calculate the size D_2 on the dashed lines in Figure 6 and plot them in Figures 7(a), (b). We determine that D_2 discontinuously changes against ϕ_0 and λ at the phase boundaries, similar to that in model 1 shown in Figures 4(a), (b). Moreover, the phase boundary is also not as clear because of the same reason as that for model 1. In fact, the surface shape at the phase boundary between the two circular and stripe domains is not always stable in model 2, similar to that in model 1. Figure 7(c) also shows that S_2/N_B discontinuously changes; however, the gap is very small, and these two phases are hence separated by a weak first-order transition. The phase boundary between the two circular and the random domains is also expected to be continuous in model 2. The boundaries of one circular to two circulars and one circular to stripe are also

not as clear, and the boundary of one circular to random is continuous.

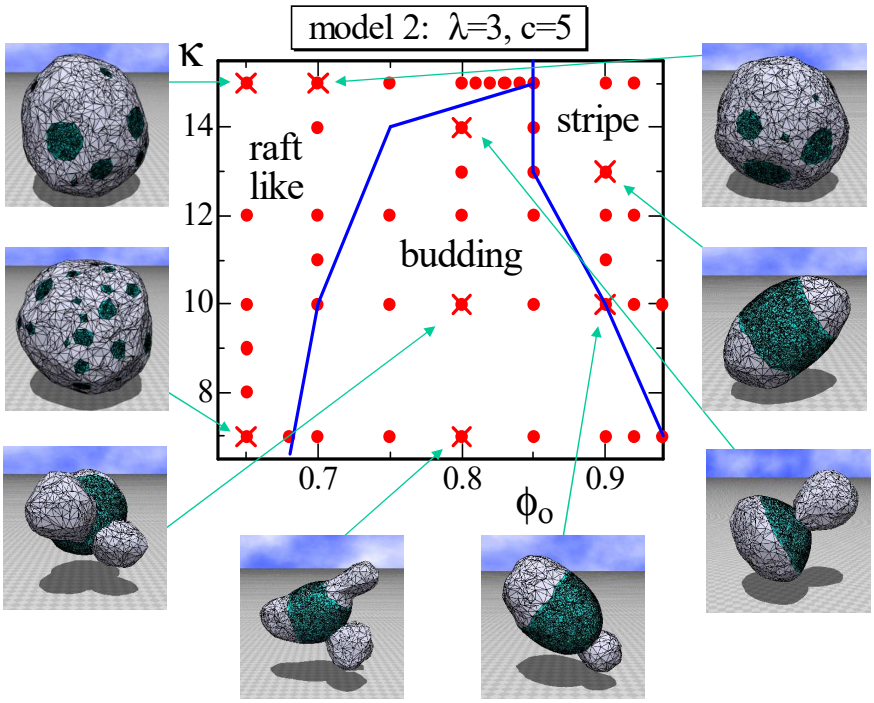

Fig. 8. A phase diagram of model 2 on the $\kappa-\phi_o$ plane at $\lambda=3$ and $c=5$ and the snapshots of surfaces. The solid lines on the phase diagram denote the phase boundaries. The solid circles (•) denote the data points of the simulations for the phase boundaries.

Another difference between model 1 and model 2, other than the appearance of the stable one circular domain, is the raft-like domain and the budding domain. More precisely, the budding domain can also be seen in model 1; however, it is more clear in model 2. The phase diagram of model 2 on the $\kappa-\phi_0$ plane is drawn in Figure 8. The parameter λ is fixed to $\lambda=3$, which is relatively large compared with the previous one assumed in the simulations for Figures 3 and 6. Consequently, the energy λS_0, which is the line tension energy, at the phase boundary between L_0 and L_d becomes large in the region where κ is relatively small. This is the reason why the budding domain appears on this $\kappa-\phi_0$ plane in Figure 8. Note that the budding domain in some of the budding surfaces goes inside the surface and some of them self-intersect because no self-avoiding interaction is assumed. Figure 8 also shows that the raft-like domain is stable in the relatively large κ region, where the surface hardly deforms. The reason why the raft domains, which are multi-circular domains, appear only at the region of small ϕ_0 is because the multi-circular domains are more energetically favourable than the stripe domain. Indeed, the effective bending rigidity $\kappa\kappa_{ij}$ and hence κS_2 become very large on the large connected L_o domain, such as the stripe domain, where the line tension energy λS_0 is relatively small. Note that S_0 has a non-zero positive value only on the boundary bonds between L_o and L_d, while S_2 has a non-zero value on all of the

bonds. Moreover, note that the boundary length between L_o and L_d becomes longer (shorter) if the total number of circular domains increases (decreases), whereas the areas of L_o and L_d remain constant and are independent of the total number of L_o domains.

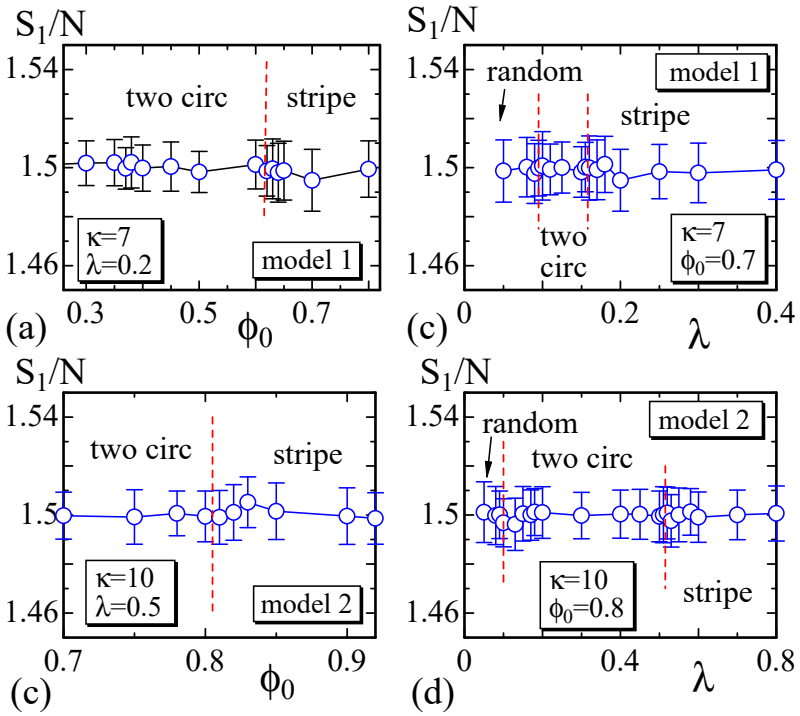

Fig. 9. (a) The Gaussian energy S_1/N vs. ϕ_0 at $\lambda=0.2$, (b) S_1/N vs. λ at $\phi_0=0.7$ for model 1, (c) S_1/N vs. ϕ_0 at $\lambda=0.5$, and (d) S_1/N vs. λ at $\phi_0=0.8$ for model 2. The data in (a) and (b) ((c) and (d)) are obtained on the dashed lines in Figure 3 (Figure 6).

Finally, we show that S_1/N satisfies the relation $S_1/N=1.5$, which is expected by the scale invariance of Z in Eq. (6) [29]. As described in Section 2, the bond length is expected to be well defined in the sense that the mean bond length is constant on the surface, although this constant varies depending on the domains or the domain boundary to which the bond belongs. The data in Figures 9(a), (b) are obtained on the dashed lines in Figure 3, and those in Figures 9(c), (d) are obtained on the lines in Figure 6. These data shown in Figure 9 indicate that the simulations including the energy discretization are successful.

5 Summary and conclusion

We have studied the phase separation of the three-component membrane with DPPC, DOPC, and cholesterol using a Finsler geometry (FG) surface model.

The FG model is obtained from the Helfrich-Polyakov (HP) model for membranes by replacing the surface metric with a general one $g_{ab} \neq \delta_{ab}$, which can be called the Finsler metric. In other words, we have extended the HP model to explain the morphological changes of the three-component membranes in the context of FG modelling. This new model includes a new degree of freedom σ, which represents the liquid-ordered (L_o) and liquid-disordered (L_d) domains. The results obtained from Monte Carlo (MC) simulations are consistent with the experimental results that have been reported in the literature. We confirm the phase separation of the L_o and L_d domains on the surface and that the surface shows a variety of morphologies, such as the two circular domain, the stripe domain, the raft domain, and the budding domain.

The line tension energy, which has been used for understanding the morphological changes, simply corresponds to the aggregation energy term λS_0 in our model. Indeed, the value of S_0 is only the total number of bonds on the boundary between L_o and L_d in our new model. Moreover, the fact that λS_0 is simply the line tension energy implies that the line tension originates from the interaction between the domains because the interaction between the variables σ in S_0 describes the interaction between the domains. This interaction is closely connected to the property of the new model that the surface strength, such as the surface tension and the bending rigidity, is dependent on the bond position on the surface. This property arises from the interaction between σ and $\mathbf{r}$ introduced via the Finsler metric.

We acknowledge Hideo Sekino, Andrey Shobukhov, Giancarlo Jug and Andrei Maximov for discussions. This work is supported in part by JSPS KAKENNHI Number 26390138.

A Finsler geometry modelling

A.1 Discrete surface model

To obtain the discrete model from the continuous surface model introduced in Section 2.1, we assume that the surface is triangulated in $\Re^3$. The Hamiltonian is defined on the triangulated surfaces, which are composed of three simplexes such as vertices, bonds, and triangles. Thus, all physical quantities, including Hamiltonians and the metric function, are defined on these simplexes labelled by integers. For example, the vertex position $\mathbf{r}_i$ is defined at the vertex i, the bond length ℓ_{ij} is defined on the bond ij, and the elements of g_{ab} are defined on the triangle Δ. Note that the variable $\mathbf{r}$ is considered as a mapping from the parameter space M to $\Re^3$.

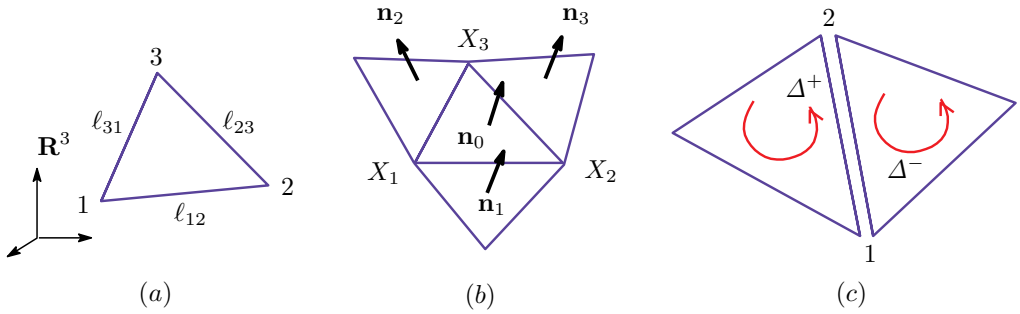

(a) (b) (c)

Fig. A.1. (a) A triangle Δ included in a triangulated sphere in $\Re^3$; (b) the three nearest neighbour triangles of Δ and the unit normal vectors $\mathbf{n}_0$, $\mathbf{n}_1$, $\mathbf{n}_2$ and $\mathbf{n}_3$; and (c) the triangle orientation that defines the direction-dependent bond potential $\gamma_{12}\ell_{12}^2$ and $\gamma_{21}\ell_{21}^2$ of the bond 12, where $\ell_{12}=\ell_{21}$.

We start with the discrete metric g_{ab} such that

$$g_{ab} = \begin{pmatrix} 1/\rho & 0 \\ 0 & \rho \end{pmatrix}, \quad \rho > 0, \tag{A.1}$$

where ρ is a function on a triangle $\Delta(\subset \Re^3)$ (see Figure A.1(a)). More precisely, the elements of g_{ab} are functions on the triangle $\Delta_M(\subset M)$, where M is the aforementioned two-dimensional space M (independent of $\Re^3$). We assume that M is also triangulated by the triangles Δ_M. On this Δ_M, an orthogonal coordinate can be taken for any one of three vertices [14]. For this reason, the metric g_{ab} can be diagonalizable. The inequality $\rho>0$ in Eq. (A.1) is necessary for the positivity of the bond length. This metric depends only on x and is independent of y, and hence, it simply corresponds to the Riemannian metric. Indeed, this metric in Eq. (A.1) comes from the most general one, such as $g_{ab}=\begin{pmatrix} E & F \\ F & G \end{pmatrix}$, with the functions of $E>0,\ G>0, EG-F^2>0$. By assuming $F=0$, we have $g_{ab}=\begin{pmatrix} E & 0 \\ 0 & G \end{pmatrix}=E\begin{pmatrix} 1 & 0 \\ 0 & G/E \end{pmatrix}\simeq\begin{pmatrix} 1 & 0 \\ 0 & \rho^2 \end{pmatrix}\simeq\begin{pmatrix} 1/\rho & 0 \\ 0 & \rho \end{pmatrix}$, where $\rho^2=G/E$ and the symbol "$\simeq$" denotes conformally equivalent. Note that this expression of g_{ab} depends on the local coordinates on Δ, and therefore, the expression of g_{ab} implicitly depends on the vertex of Δ because the coordinate origin is located on one of the vertices of Δ. In the discrete models that have been studied thus far, the Euclidean metric $g_{ab}=\delta_{ab}$ (or the induced metric $g_{ab}=\partial_a\mathbf{r}\cdot\partial_b\mathbf{r}$) is always assumed as mentioned above, and it has been reported that the model for polymerized membranes undergoes a discontinuous or a continuous transition between the crumpled phase and the smooth phase [32,33,34,35].

Let the vertex $\mathbf{r}_1$ of the central triangle Δ in Figure A.1(b) be the local coordinate origin in this Δ. By replacing

$$\begin{aligned}
&\int \sqrt{g} d^2x \to \sum_{\Delta}, \\
&\frac{\partial \mathbf{r}}{\partial x_1} \to \mathbf{r}_2 - \mathbf{r}_1, \quad \frac{\partial \mathbf{r}}{\partial x_2} \to \mathbf{r}_3 - \mathbf{r}_1, \\
&\frac{\partial \mathbf{n}}{\partial x_1} \to \mathbf{n}_0 - \mathbf{n}_2, \quad \frac{\partial \mathbf{n}}{\partial x_2} \to \mathbf{n}_0 - \mathbf{n}_1,
\end{aligned} \tag{A.2}$$

we have

$$\begin{aligned}
S_1 &= \sum_{\Delta} S_1(\Delta) = \sum_{\Delta} \left(\rho \ell_{12}^2 + \frac{1}{\rho} \ell_{13}^2 \right), \\
S_2 &= \sum_{\Delta} S_2(\Delta) = \sum_{\Delta} \left[\rho (1 - \mathbf{n}_0 \cdot \mathbf{n}_1) + \frac{1}{\rho} (1 - \mathbf{n}_0 \cdot \mathbf{n}_2) \right],
\end{aligned} \tag{A.3}$$

where $\mathbf{n}_i (i = 1, 2, 3)$ are the unit normal vectors shown in Figure A.1(b). The symbol $\ell_{ij} (= \ell_{ji})$ is defined by $\ell_{ij} = |\mathbf{r}_j - \mathbf{r}_i|$. Note that the unit normal vector also represents the surface orientation; indeed, $\mathbf{n}_0$ is defined by $\mathbf{n}_0 = \vec{\ell}_{12} \times \vec{\ell}_{13} / |\vec{\ell}_{12} \times \vec{\ell}_{13}|$ for example.

We have three possible coordinate origins in the triangles. For this reason, S_1 and S_2 can be symmetrized by including the terms that are cyclic permutations, such as $1 \to 2$, $2 \to 3$, $3 \to 1$ for ℓ_{ij}, $\mathbf{n}_i$ and ρ_i. Summing over all possible terms and multiplying by a factor of $1/3$, we obtain

$$\begin{aligned}
S_1 &= \frac{1}{3} \sum_{\Delta} \left[\left(\rho_1 + \frac{1}{\rho_2} \right) \ell_{12}^2 + \left(\rho_2 + \frac{1}{\rho_3} \right) \ell_{23}^2 + \left(\rho_3 + \frac{1}{\rho_1} \right) \ell_{31}^2 \right], \\
S_2 &= \frac{1}{3} \sum_{\Delta} \left[\left(\rho_1 + \frac{1}{\rho_2} \right) (1 - \mathbf{n}_0 \cdot \mathbf{n}_1) + \left(\rho_2 + \frac{1}{\rho_3} \right) (1 - \mathbf{n}_0 \cdot \mathbf{n}_3) \right. \\
&\qquad \left. + \left(\rho_3 + \frac{1}{\rho_1} \right) (1 - \mathbf{n}_0 \cdot \mathbf{n}_2) \right],
\end{aligned} \tag{A.4}$$

where $\rho_i (i = 1, 2, 3)$ are defined on the triangle Δ. The reason for why these three different functions ρ_i are included is because the expression for g_{ab} generally depends on the local coordinate as mentioned above. More precisely, ρ_i is the element of g_{ab} on Δ where the coordinate origin is located at vertex i. For arbitrary g_{ab}, we always have the metric of the form in Eq. (A.1) by the same procedure as described above.

Here, we further simplify the model by assuming that

$$\rho_1 = \rho_2 = \rho_3 (= \rho_\Delta). \tag{A.5}$$

Thus, we have the expressions

$$\begin{aligned} S_1 &= \frac{1}{3} \sum_\Delta \left(\rho_\Delta + \frac{1}{\rho_\Delta} \right) \left(\ell_{12}^2 + \ell_{23}^2 + \ell_{31}^2 \right), \\ S_2 &= \frac{1}{3} \sum_\Delta \left(\rho_\Delta + \frac{1}{\rho_\Delta} \right) (1 - \mathbf{n}_0 \cdot \mathbf{n}_1 + 1 - \mathbf{n}_0 \cdot \mathbf{n}_2 + 1 - \mathbf{n}_0 \cdot \mathbf{n}_3). \end{aligned} \tag{A.6}$$

Replacing the sum over triangles $\sum_\Delta$ with the sum over bonds $\sum_{ij}$, we obtain

$$\begin{aligned} S_1 &= \frac{1}{3} \sum_{ij} \left(\rho_i + \frac{1}{\rho_i} + \rho_j + \frac{1}{\rho_j} \right) \ell_{ij}^2, \\ S_2 &= \frac{1}{3} \sum_{ij} \left(\rho_i + \frac{1}{\rho_i} + \rho_j + \frac{1}{\rho_j} \right) (1 - \mathbf{n}_i \cdot \mathbf{n}_j). \end{aligned} \tag{A.7}$$

Note that S_1 and S_2 defined by the sum over triangles $\sum_\Delta$ in Eq. (A.6) are exactly same as those defined by the sum over bonds $\sum_{ij}$ in Eq. (A.7), and the difference is only in their expressions. Additionally, note that the suffixes i, j of ℓ_{ij} in Eq. (A.7) denote the bond ij, whereas those of ρ_i and ρ_j denote the two neighbouring triangles i and j of the bond ij. Thus, we finally have

$$\begin{aligned} &S(\mathbf{r}, \sigma) = S_1 + \kappa S_2, \\ &S_1 = \sum_{ij} \gamma_{ij} \ell_{ij}^2, \quad S_2 = \sum_{ij} \kappa_{ij} (1 - \mathbf{n}_i \cdot \mathbf{n}_j), \end{aligned} \tag{A.8}$$

with

$$\gamma_{ij} = \kappa_{ij} = \frac{c_i + c_j}{4}, \quad c_i = \rho_i + \frac{1}{\rho_i}, \tag{A.9}$$

where the irrelevant numerical factor $1/3$ is replaced by $1/4$ in the final expressions for S_1 and S_2.

Note that γ_{ij} ($\kappa\kappa_{ij}$) can be called the effective surface tension (effective bending rigidity) on the bond between vertices i and j. It must be emphasized that the quantities γ_{ij} and κ_{ij} are independent of the bond direction, or in other words, these are symmetric under the exchange of i and j, and for this reason, γ_{ij} and κ_{ij} are considered as the quantities defined on the bond ij. Indeed, from the expression given in Eq. (A.9), we have

$$\gamma_{ij} = \gamma_{ji}, \quad \kappa_{ij} = \kappa_{ji}. \tag{A.10}$$

Therefore, the physical quantities $\gamma_{ij}\ell_{ij}^2$ in S_1 and $\kappa_{ij}(1-\mathbf{n}_i\cdot\mathbf{n}_j)$ in S_2 of Eq. (A.8) are well defined in the sense that these quantities are symmetric under the exchange of ij. The reason why we need this symmetry in the physical quantities $\gamma_{ij}\ell_{ij}^2$ and $\kappa_{ij}(1-\mathbf{n}_i\cdot\mathbf{n}_j)$ is because these quantities correspond to the energies for the expansion and bending of the surface at the bond ij, and these energies are independent of the bond direction such as the one from i to j or the reverse. Thus, the symmetry property in Eq. (A.10) allows us to call γ_{ij} and $\kappa\kappa_{ij}$ the effective surface tension and the effective bending rigidity on the bond ij, respectively. However, as we will show in the next subsection, γ_{ij} and κ_{ij} are not symmetric in general (see Figure A.1(c)). Moreover, note that this problem of whether γ_{ij} and κ_{ij} are symmetric arises only when γ_{ij} and κ_{ij} depend on the functions ρ_i and ρ_j on the two neighbouring triangles i and j. This is in sharp contrast to the case where γ_{ij} and κ_{ij} depend only on the quantity defined on the vertices [10], where γ_{ij} and κ_{ij} are always symmetric. This exchange symmetry/asymmetry reflects the orientation symmetry/asymmetry, which will be discussed in the next subsection.

A.2 Finsler geometry model

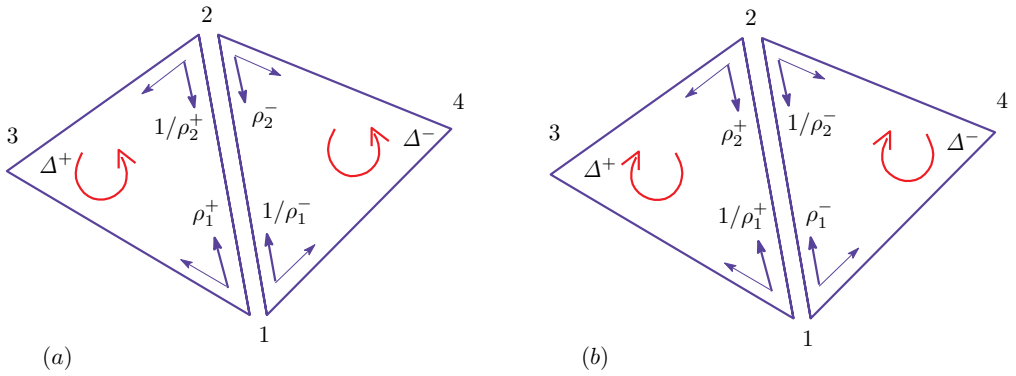

Fig. A.2. Local coordinate origins of the triangles Δ^+ and Δ^- for $S_1(\ell_{12})$, and the elements of γ_{12} and γ_{21} of the configurations of (a) the original and (b) the inside out (inside view).

In this subsection, we show that the discrete surface models constructed above are well defined only in the context of Finsler geometry modelling [10]. For this purpose, we should first remind ourselves of the fact that the symmetry properties in Eq. (A.10) can be observed in the model only under the condition of Eq. (A.5). This symmetry is not present in the model of Eq. (A.4). To show the breakdown of the symmetry of Eq. (A.10) in the model of Eq. (A.4) in more detail, we replace the sum over triangles $\sum_\Delta$ of S_1 and S_2 in Eq. (A.4) with the sum over bonds $\sum_{ij}$ before the condition of Eq. (A.5) is imposed. In this new expression of S_1, which is expressed by the sum over bonds $\sum_{ij}$, the Gaussian bond potential for the bond 12, which is shared by the triangles Δ^+ and Δ^- as in Figure A.2(a) for example, is given by

$$S_1(\ell_{12}) = (1/3)\left(\rho_1^+ + \frac{1}{\rho_2^+} + \rho_2^- + \frac{1}{\rho_1^-}\right)\ell_{12}^2 \sim \gamma_{12}\ell_{12}^2. \tag{A.11}$$

In this expression, the former half $S_1^+(\ell_{12}) = (1/3)\left(\rho_1^+ + 1/\rho_2^+\right)\ell_{12}^2$ is the contribution from Δ^+, and the latter half $S_1^-(\ell_{12}) = (1/3)\left(\rho_2^- + 1/\rho_1^-\right)\ell_{12}^2$ is the contribution from Δ^-. However, it is clear that γ_{12} and hence $S_1(\ell_{12})$ in Eq. (A.11) are not symmetric under the change of surface orientation. In fact, we have

$$\bar{S}_1(\ell_{12}) = (1/3)\left(\rho_2^+ + \frac{1}{\rho_1^+} + \rho_1^- + \frac{1}{\rho_2^-}\right)\ell_{12}^2 \sim \gamma_{21}\ell_{12}^2 \tag{A.12}$$

for the opposite orientation (see Figure A.2(b)). In Eq. (A.12), we write the coefficient of ℓ_{12}^2 by γ_{21} because it is obtained from γ_{12} in Eq. (A.11) by exchanging the suffixes 1 and 2. It is also easy to show that $\gamma_{12} \neq \gamma_{21}$ and hence $S_1(\ell_{12})$ are not always identical to $\bar{S}_1(\ell_{12})$ in general.

Thus, we find that the asymmetry $\gamma_{12} \neq \gamma_{21}$ means that $S_1(\ell_{12})$ is not invariant under the orientation exchange. From this, we can see that the Gaussian bond potential energy (and also the bending energy) of the bond 12 of one surface configuration differs from that of the opposite orientation configuration. However, we have no reason for the difference in S_1 for two surfaces with different orientations. Thus, the model defined by Eq. (A.4), which is orientation asymmetric, is ill defined in the context of conventional surface modelling.

Moreover, we have to remark that the model defined by Eq. (A.8), which is orientation symmetric, is also ill defined. The reason for this ill definedness is that the bond length squares calculated with ρ^+ in Δ^+ is not always identical to the one calculated with ρ^- in Δ^- in Figure A.2(a), where $\rho_1^\pm = \rho_2^\pm$ in the model of Eq. (A.8). Indeed, the metric on Δ^+ is given by $g_{ab} = \begin{pmatrix} 1/\rho^+ & 0 \\ 0 & \rho^+ \end{pmatrix}$, where the coordinate origin is at the vertex 1. Then, we have the bond length squares $(1/\rho^+)\,\ell_{12}^2$ for the bond 12 with respect to the metric g_{ab}, and changing the vertex origin from 1 to 2, we also have $\rho^+\ell_{12}^2$. Thus, summing over these two expressions without the coefficient 1/2, we have $(1/\rho^+ + \rho^+)\,\ell_{12}^2$ for the bond length squares. Through the same procedure, we have $(1/\rho^- + \rho^-)\,\ell_{12}^2$ from Δ^-. These two square lengths of the bond 12 must be the same. However, we have

$$\frac{1}{\rho^+} + \rho^+ \neq \frac{1}{\rho^-} + \rho^- \tag{A.13}$$

because $\rho^+ \neq \rho^-$ in general. The edge length of triangles should uniquely be given as the basic requirement even in the discrete models. Therefore, in a

model construction on the triangulated lattices, we always obtain an ill-defined discrete model if we start with an arbitrary Riemannian metric in which the elements are defined on the triangles. Note that the bond "length" used here is the length with respect to g_{ab} on $\Delta^{\pm}$ and is different from the Euclidean bond length ℓ_{ij} (also note that g_{ab} is simply a Riemannian metric at this stage).

However, these ill-defined models in Eqs. (A.4) and (A.8) become well defined in the context of Finsler geometry [10,11,12]. In this context, the bond length calculated with g_{ab} on the triangle Δ^{+} can be considered as the direction-dependent length from 1 to 2, and the one calculated with g_{ab} on Δ^{-} can be considered as the length from 2 to 1 (Fig. A.2(a)). Therefore, the inequality in Eq. (A.13) is satisfied in general. Moreover, the aforementioned quantities $S_1^{+}(\ell_{12})$ and $S_1^{-}(\ell_{12})$ in Eqs. (A.11) and (A.12) are meaningful because these quantities are also considered as direction dependent in the Finsler geometry context (Fig. A.1(c)).

References

[1] Veatch S.L. and Keller S.L., Miscibility Phase Diagrams of Giant Vesicles Containing Sphingomyelin, *Phys. Rev. Lett.* **2005**, *94*, 148101(1-4).

[2] Yanagisawa M., Imai M., and Taniguchi T., Shape Deformation of Ternary Vesicles Coupled with Phase Separation, *Phys. Rev. Lett.* **2008**, *100*, 148102(1-4).

[3] Yanagisawa M., Imai M., and Taniguchi T., Periodic modulation of tubular vesicles induced by phase separation, *Phys. Rev. E* **2010**, *82*, 051928(1-9).

[4] Gutlederer E., Gruhn T. and Lipowsky R., Polymorphism of vesicles with multi-domain patterns, *Soft Matter* **2009**, *5*, 3303-3311.

[5] Jülicher P. and Lipowsky R., Domain-induced budding of vesicles, *Phys. Rev. Lett.* **1993**, *70*, 2964-2967.

[6] Jülicher P. and Lipowsky R., Shape transformations of vesicles with intramembrane domains, *Phys. Rev. E* **1996**, *53*, 2670-2683.

[7] Jug G., Theory of the thermal magnetocapacitance of multicomponent silicate glasses at low temperature, *Philos. Mag.* **2004**, *84* (33), 3599-3615.

[8] Polyakov A.M., Fine structure of strings, *Nucl. Phys. B* **1986**, *268*, 406-412.

[9] Helfrich W., Elastic Properties of Lipid Bilayers: Theory and Possible Experiments, *Z. Naturforsch* **1973**, *28c*, 693-703.

[10] Koibuchi H. and Sekino H., Monte Carlo studies of a Finsler geometric surface model, *Physica A* **2014**, *393*, 37-50.

[11] Matsumoto M., Keiryou Bibun Kikagaku (in Japanese), Shokabo: Tokyo, Japan, 1975.

[12] Bao D., Chern S. -S., Shen Z., An Introduction to Riemann-Finsler Geometry, GTM 200, Springer: New York, USA, 2000.

[13] Doi M. and Edwards S.F., *The Theory of Polymer Dynamics*, (Oxford University Press, 1986).

[14] David F., Geometry and Field Theory of Random Surfaces and Membranes, In *Statistical Mechanics of Membranes and Surfaces, Second Edition*; Eds. Nelson D., Piran T., and Weinberg S., World Scientific: Singapore, 2004; pp.149-209.

[15] Paczuski M., Kardar M. and Nelson D.R., Landau Theory of the Crumpling Transition, *Phys. Rev. Lett.* **1988**, *60*, 2638-2640.

[16] Kantor Y. and Nelson D.R., Phase transitions in flexible polymeric surfaces, *Phys. Rev. A* **1987**, *36*, 4020-4032.

[17] Peliti L. and Leibler S., Effects of Thermal Fluctuations on Systems with Small Surface Tension, *Phys. Rev. Lett.* **1985** *54* 1690-1693.

[18] David F. and Guitter E., Crumpling Transition in Elastic Membranes: Renormalization Group Treatment, *Europhys. Lett.* **1988**, *5*, 709-714.

[19] Nelson D., The Statistical Mechanics of Membranes and Interfaces, In *Statistical Mechanics of Membranes and Surfaces, Second Edition*; Eds. Nelson D., Piran T., and Weinberg S., World Scientific: Singapore, 2004; pp.1-17.

[20] Bowick M. and Travesset A., he statistical mechanics of membranes, *Phys. Rep.* **2001**, *344*, 255-308.

[21] Wiese K.J., Polymerized Membranes, a Review, in *Phase Transitions and Critical Phenomena 19*, eds. C. Domb, and J.L. Lebowitz (Academic Press, London, 2000) pp.253-498.

[22] Gompper G. and Kroll D.M., Triangulated-surface models of fluctuating membranes. In *Statistical Mechanics of Membranes and Surfaces, Second Edition*; Eds. Nelson D., Piran T., and Weinberg S., World Scientific: Singapore, 2004; pp.359-426.

[23] Baumgärtner A. and Ho J.-S., Crumpling of fluid vesicles, *Phys. Rev. A* **1990**, *41*, 5747-5750(R).

[24] Ho J.-S. and Baumgärtner A., Simulations of Fluid Self-Avoiding Membranes, *Europhys. Lett.* **1990**, *12*, 295-300.

[25] Catterall S.M., Extrinsic curvature in dynamically triangulated random surfaces, *Phys. Lett. B* **1989**, *220*, 207-214.

[26] Catterall S.M., Kogut J.B., and Renken R.L., Numerical study of field theories coupled to 2D quantum gravity, *Nucl. Phys. B Proc. Suppl.* **1992**, *25*, 69-86.

[27] Ambjörn J., Irbäck A., Jurkiewicz J., Petersson B., The theory of dynamical random surfaces with extrinsic curvature, *Nucl. Phys. B* **1993**, *393*, 571-600.

[28] Noguchi H., Membrane Simulation Models from Nanometer to Micrometer Scale, *J. Phys. Soc. Jpn.* **2009**, *78*, 041007(1-9).

[29] Wheater J.F., Random surfaces: from polymer membranes to strings, *J. Phys. A Math. Gen.* **1994**, *27*, 3323-3353.

[30] Metropolis N., Rosenbluth A.W., Rosenbluth M.N. and Teller A.H., Equation of State Calculations by Fast Computing Machines, *J. Chem. Phys.* **1953**, *21*, 1087-1092.

[31] Landau D.P., Finite-size behavior of the Ising square lattice, *Phys. Rev. B* **1976**, *13*, 2997-3011.

[32] Kownacki J-P. and Diep H.T., First-order transition of tethered membranes in three-dimensional space, *Phys. Rev. E* **2002**, *66*, 066105(1-6).

[33] Kownacki J.-P. and Mouhanna D., Crumpling transition and flat phase of polymerized phantom membranes, *Phys. Rev. E* **2009**, *79*, 040101(R)(1-4).

[34] Essafi K., Kownacki J.-P. and Mouhanna D., First-order phase transitions in polymerized phantom membranes, *Phys. Rev. E* **2014**, *89*, 042101(1-5).

[35] Cuerno R., G.C. R., Gordillo-Guerrero A., Monroy P., and Ruiz-Lorenzo J.J., Universal behavior of crystalline membranes: crumpling transition and Poisson ratio of the flat phase, *Phys. Rev. E* **2016**, *93*, 022111(1-9).